Simulation of immiscible two-phase flows based on a kinetic diffuse interface approach

Tao Chen, Victor Chéron, Zhaoli Guo, Jorge César C Brändle de Motta, Thibault Menard, Lian-Ping Wang

Simulation of immiscible two-phase flows based on a kinetic diffuse interface approach

Tao Chen[1,2], Victor Chéron[3], Zhaoli Guo[4], Jorge César Brändle de Motta[3],
Thibault Ménard[3] and Lian-Ping Wang[2,5]

[1] SKLTCS, College of Engineering, Peking University, Beijing 100871, China

[2] Department of Mechanics and Aerospace Engineering, Southern University of Science and Technology,
Shenzhen 518055, Guangdong, China

[3] COmplexe de Recherche Interprofessionnel en Aéothermochimie (CORIA),
Université de Rouen Normandie, CNRS, INSA de Rouen, Saint-Étienne du Rouvray, France

[4] State Key Laboratory of Coal Combustion, School of Energy and Power Engineering,
Huazhong University of Science and Technology, Wuhan 430074, Hubei, China

[5] Department of Mechanical Engineering, University of Delaware, Newark, DE 19716-3140, USA

1601111553@PKU.EDU.CN; CHERONV@CORIA.FR; ZLGUO@HUST.EDU.CN; JORGE.BRANDLE@CORIA.FR;
TMENARD@CORIA.FR; LWANG@UDEL.EDU

Keywords: immiscible two-phase flow, homogeneous isotropic turbulence, gas kinetic scheme, diffuse interface

Abstract

A direct numerical simulation (DNS) code is developed to simulate immiscible two-phase flows based on the recently developed discrete unified gas-kinetic scheme (DUGKS). This scheme simulates hydrodynamic equations of the quasi-incompressible Cahn-Hilliard-Navier-Stokes system by the use of two mesoscopic distributions and the proper design of their equilibrium distributions and source terms. Several immiscible two-phase flows are used to validate the scheme in both 2D and 3D, including a stationary droplet in 2D and 3D, the Rayleigh-Taylor flows, and two-phase homogeneous isotropic decaying turbulence. The results obtained by DUGKS are compared carefully to these from the literature and the ARCHER code, *i.e.*, a Coupled Level Set - Volume of Fluid (CLSVOF) method. The comparisons indicate that DUGKS is a promising scheme for direct numerical simulations of immiscible two-phase flows.

Introduction

Immiscible two-phase flows occur in a variety of industrial processes such as emulsion, sprays, boiling, and cavitation. These flows contain fluid-fluid interfaces involving extensive topological changes which are coupled with flow fluctuations at different scales. There detailed flow features are difficult to be treated experimentally and computationally. In recent years, numerical methods have served as a vital research tool for probing flow structures and nonlinear dynamics in these complex flows. Most of these simulations were performed based on the continuum (or macroscopic) Navier-Stokes equations. Since the 1990s, mesoscopic methods based on the Boltzmann equation, such as the lattice Boltzmann method and gas kinetic schemes, have also been developed and applied to simulate these complex flows, with various degrees of success.

In this paper, we consider a relatively new gas kinetic scheme known as the discrete unified gas kinetic scheme (DUGKS) (Guo *et al.* 2013, 2015). Based on the Boltzmann-BGK equation, Guo *et al.* developed the DUGKS scheme by combining the advantages of both the lattice Boltzmann method (LBM) and unified gas kinetic scheme (UGKS). In DUGKS, a model Boltzmann equation is solved using an accurate finite volume formulation coupling tightly kinetic particle transport and particle collisions. Compared to the lattice Boltzmann scheme, DUGKS can more easily incorporate irregular meshes and different kinetic particle velocity models. The scheme has been applied to simulate single-phase homogeneous isotropic turbulence (Wang *et al.* 2016) and wall bounded turbulent flow (Bo *et al.* 2017).

Here we further explore the capabilities of DUGKS by incoporating non-ideal molecular interaction forces using the diffuse interface formulation, so that the dynamics of fluid-fluid interfaces can be simulated. Preliminary two-dimensional simulations of the Rayleigh-Taylor instability, using this approach, have been reported in Zhang *et al.* (2018).

The primary objective of this work is to develop a three-dimensional implementation of this two-phase DUGKS ap-

proach, and validate the code by comparing the results from the literature and from the CLSVOF method employed by in the ARCHER code (Menard *et al.* 2007). The ARCHER code has been chosen because of its robustness, maturity and complementarity comparing to DUGKS. Indeed, this code solves the Navier-Stokes equations with a consistent finite volume scheme and considers a sharp interface approach. """""" The second objective, by comparing two completely different approaches (DUGKS and ARCHER), is to provide new benchmark data for several immiscible two-phase flows. The rest of the paper is organized as follows. First, the quasi-incompressible Cahn-Hilliard-Navier-Stokes (CHNS) system is briefly introduced, along with the DUGKS implementation of the system. Then a few immiscible two-phase flows are considered, in order of complexity: (a) a two-dimensional stationary droplet, (b) a three dimensional stationary droplet respectively, (c) 2D Rayleigh-Taylor flows under unstable conditions, (d) 3D Rayleigh-Taylor instability, and (e) 3D two-phase decaying homogeneous isotropic turbulence. Cases (a) and (b) have been simulated many times in the literature but the individual interaction terms in the diffuse interface approach (also known as the phase field method) used in DUGKS will be analyzed more thoroughly here. In cases (c), (d), and (e), the results from DUGKS and ARCHER will be compared more systematically. The results in case (e) also provide some physical insight into the secondary breakup of a drop in a background turbulent flow.

Quasi-incompressible phase-field approach

In the phase field approach, an order parameter ϕ is used to distinguish the different fluids. This phase field varies continuously across the interfacial region separating the two fluids. A Landau free-energy function (also known as the mixing energy) is defined as

$$F(\phi) = \int_V \left[\psi(\phi) + \frac{\kappa}{2}|\nabla\phi|^2\right] dV, \tag{1}$$

where the first term $\psi(\phi)$ represents the free-energy density of molecules in the interfacial region interacting with the bulk fluids, the second term provides interaction energy among molecules within the interfacial region. Both contribute to the interface energy which defines a surface tension. κ is the cofficient of the surface tension, and V is the control volume. For isothermal flows considered here, the following double-well energy density is used,

$$\psi(\phi) = \beta(\phi-\phi_A)^2(\phi-\phi_B)^2. \tag{2}$$

where ϕ_A and ϕ_B are constants corresponding to the equilibrium state of the order parameters of the bulk fluids A and B, respectively. Here the interaction energy density among molecules in either bulk region has been excluded, and will be modeled by a separate hydrodynamic pressure term in Eq. (8). The parameters ϕ_A, ϕ_B, β and κ together determine the interfacial thickness W and surface tension σ,

$$W = \frac{1}{\phi_A-\phi_B}\sqrt{8\kappa/\beta}, \quad \sigma = \frac{|\phi_A-\phi_B|^3}{6}\sqrt{2\kappa\beta}. \tag{3}$$

The variation of the free-energy function $F(\phi)$ with respect to ϕ yields the chemical potential μ_ϕ,

$$\begin{aligned}\mu_\phi &\equiv \frac{\delta F}{\delta\phi} = \frac{\delta\psi}{\delta\phi} - \kappa\nabla^2\phi \\ &= 4\beta(\phi-\phi_A)(\phi-\phi_B)\left(\phi - \frac{\phi_A+\phi_B}{2}\right) - \kappa\nabla^2\phi.\end{aligned} \tag{4}$$

For a flat surface at equilibrium, the profile across the interface can be obtained by solving $\mu_\phi(\phi) = 0$, which yields

$$\phi(\zeta) = \frac{\phi_A+\phi_B}{2} + \frac{\phi_A-\phi_B}{2}\tanh\left(\frac{2\zeta}{W}\right), \tag{5}$$

where ζ is the normal coordinate of the flat interface.
The evolution of ϕ is typically governed by the Cahn-Hilliard equation,

$$\frac{\partial\phi}{\partial t} + \nabla\cdot(\phi\boldsymbol{u}) = \nabla\cdot(\lambda\nabla\mu_\phi), \tag{6}$$

where $\boldsymbol{u}$ is the macroscopic (continuum) fluid velocity and λ is the mobility. The interfacial diffusion flux is assumed to be proportional to the gradient of the chemical potential.
In quasi-incompressible phase-field multiphase flow model, the hydrodynamic equations are given by Zhang *et al.* (2018)

$$\nabla\cdot\boldsymbol{u} = -\gamma\nabla\cdot(\lambda\nabla\mu_\phi), \tag{7}$$

$$\rho\left(\frac{\partial\boldsymbol{u}}{\partial t} + \boldsymbol{u}\cdot\nabla\boldsymbol{u}\right) = -\nabla p + \nabla\cdot\left[\rho\nu\left(\nabla\boldsymbol{u} + \nabla\boldsymbol{u}^T\right)\right] + \boldsymbol{F}, \tag{8}$$

with the relation between the density ρ and the phase field ϕ, and the definition of γ,

$$\rho = \frac{\phi-\phi_B}{\phi_A-\phi_B}\rho_A + \frac{\phi_A-\phi}{\phi_A-\phi_B}\rho_B \tag{9}$$

.

$$\gamma = \frac{\rho_r - 1}{\phi_A - \phi_B\rho_r} \tag{10}$$

where p is a hydrodynamic pressure used to enforce the incompressibility condition outside the interfacial region, ν is the kinematic viscosity. ρ_A and ρ_B are the densities of the two fluids, respectively. $\boldsymbol{F}$ is the combined body force per unit volume, including the surface-tension force (modeled here as a volumetric force) $\boldsymbol{F}_s = -\phi\nabla\mu_\phi$ and other body forces $\boldsymbol{F}_b$, such as gravity. In our method, γ is a parameter related to the density ratio. The density ratio is defined as $\rho_r = \rho_A/\rho_B$. Substituting Eqs. (7), (9), and (10) into Eq. (6) yields

$$\frac{\partial\rho}{\partial t} + \nabla\cdot(\rho\boldsymbol{u}) = 0, \tag{11}$$

therefore, the mass is conserved locally in this specific quasi-incompressible model.

The DUGKS scheme

The DUGKS scheme is a mesoscopic model of the above CHNS system based on a model Boltzmann equation. Similar to the two-distribution function LBM, we introduce one

distribution function f_i to model the pressure p and momentum fields, and a second distribution function g_i to simulate the phase field ϕ. These two distribution functions satisfy the following Boltzmann equations,

$$\frac{\partial f_i}{\partial t} + \boldsymbol{\xi_i} \cdot \nabla f_i = -\frac{f_i - f_i^{eq}}{\tau_f} + F_i^f, \tag{12}$$

$$\frac{\partial g_i}{\partial t} + \boldsymbol{\xi_i} \cdot \nabla g_i = -\frac{g_i - g_i^{eq}}{\tau_g} + F_i^g, \tag{13}$$

where $f_i \equiv f_i(\boldsymbol{x}, \boldsymbol{\xi}_i, t)$ and $g_i \equiv g_i(\boldsymbol{x}, \boldsymbol{\xi}_i, t)$ are particle distribution functions with the discrete velocity $\boldsymbol{\xi}_i$ at position $\boldsymbol{x}$ and time t for the hydrodynamic variables and the order parameter, respectively. The subscript i denotes the set of discrete particle velocities, which is designed using the Gauss-Hermite quadrature for the best computational efficiency. τ_f and τ_g are the relaxation times for the distributions f and g, respectively. The key here is to design the corresponding equilibrium distribution functions f_i^{eq} and g_i^{eq}, as well as the two source terms F_i^f and F_i^g, such that the basic conservation requirements are met and the CHNS hydrodynamic equations can be recovered, to within a certain level of modeling errors.
The conservation requirements include

$$\begin{aligned} &\phi(\boldsymbol{x}, t) = \sum_{i=0}^{q-1} g_i(\boldsymbol{x}, \boldsymbol{\xi}_i, t), \quad p(\boldsymbol{x}, t) = \sum_{i=0}^{q-1} f_i(\boldsymbol{x}, \boldsymbol{\xi}_i, t), \\ &RT\rho(\boldsymbol{x}, t)\boldsymbol{u} = \sum_{i=0}^{q-1} \boldsymbol{\xi}_i f_i(\boldsymbol{x}, \boldsymbol{\xi}_i, t) \end{aligned} \tag{14}$$

The density field is determined through Eq. (9) in terms of ϕ.

The designed equilibrium distributions read

$$f_i^{eq} = \omega_i p + c_s^2 \rho s_i(\boldsymbol{u}), \quad g_i^{eq} = H_i + \phi s_i(\boldsymbol{u}) \tag{15}$$

where

$$\begin{aligned} s_i(\boldsymbol{u}) &= \omega_i \left[\frac{\boldsymbol{\xi_i} \cdot \boldsymbol{u}}{c_s^2} + \frac{(\xi_i \cdot \boldsymbol{u})^2}{2c_s^4} - \frac{\boldsymbol{u}^2}{2c_s^2} \right], \\ H_i &= \begin{cases} \phi - (1 - \omega_0)\eta\mu_\phi, & if\ i = 0 \\ \omega_i \eta \mu_\phi, & if\ i \neq 0 \end{cases}. \end{aligned} \tag{16}$$

Here η is introduced to improve numerical stability, with the mobility given as $\lambda = c_s^2 \tau_g \eta$, ω_i is the weighting coefficients. The speed of sound is given by $c_s^2 = RT$ as in the usual LBM, where T is reference temperature and R is the specific gas constant.
The source terms F_i^f and F_i^g are designed as

$$\begin{aligned} F_i^f = (\boldsymbol{\xi}_i - \boldsymbol{u}) \cdot [\boldsymbol{F}\Gamma_i \boldsymbol{u} + s_i(\boldsymbol{u}) c_s^2 \nabla \rho] \\ -\omega_i c_s^2 \rho \gamma \nabla \cdot (\lambda \nabla \mu_\phi) \end{aligned} \tag{17}$$

$$F_i^g = \frac{\phi}{c_s^2 \rho}(\boldsymbol{\xi} - \boldsymbol{u}) \cdot (\boldsymbol{F} - \nabla p)\Gamma(\boldsymbol{u}) \tag{18}$$

where $\Gamma_i(\boldsymbol{u}) = \omega_i + s_i(\boldsymbol{u})$.
Next, the discretiztion in space and time is briefly described.

The Boltzmann equations can be written in a unified form (Zhang *et al.* 2018),

$$\frac{\partial \varphi_i}{\partial t} + \boldsymbol{\xi}_i \cdot \nabla \varphi_i = \Omega_i^\varphi + F_i^\varphi \tag{19}$$

where φ=f or g, and $\Omega_i^\varphi = -(\varphi_i - \varphi_i^{eq})/\tau_\varphi$. The computational domain is divided into cells, with the center defined as $\boldsymbol{x}_j$. Integrating Eq. (19) over a control volume V_j centered at $\boldsymbol{x}_j$ from t_n to t_{n+1} and using the midpoint rule for the integration of the flux term at the cell interface and trapezoidal rule for the collision and source terms inside each cell, we can obtain

$$\begin{aligned} \varphi_i^{n+1} - \varphi_i^n + \frac{\delta t}{|V_j|} J^{n+1/2} \\ = \frac{\delta t}{2}[\Omega_i^{\varphi,n+1} + \Omega_i^{\varphi,n}] + \frac{\delta t}{2}[F_i^{\varphi,n+1} + F_i^{\varphi,n}] \end{aligned} \tag{20}$$

where

$$J^{n+1/2} = \int_{\partial V_j} (\boldsymbol{\xi} \cdot \boldsymbol{n}) \varphi_i(\boldsymbol{x}, \boldsymbol{\xi}_i, t_{n+1/2}) d\boldsymbol{S} \tag{21}$$

is the flux across the cell interface. $|V_j|$ and ∂V_j are the volume and the surface area at cell $\boldsymbol{x}_j, \boldsymbol{n}$ is the outward unit nomal vector of the surface. The cell-averaged value of the distribution function and the source term are, respectively,

$$\varphi_i^n \equiv \frac{1}{|V_j|} \int_{V_j} \varphi_i(\boldsymbol{x}, \boldsymbol{\xi}_i, t_n) d\boldsymbol{x} \tag{22}$$

$$F_i^{\varphi,n} \equiv \frac{1}{|V|} \int_{V_j} F_i^\varphi(\boldsymbol{x}_j, \boldsymbol{\xi}_i, t_n) d\boldsymbol{x} \tag{23}$$

To remove the time implicity, two linear transformations are introduced,

$$\begin{aligned} \widetilde{\varphi}_i &= \varphi_i - \frac{\delta t}{2}(\Omega_i^\varphi + F_i^\varphi) \\ &= \frac{2\tau_\varphi + \delta t}{2\tau_\varphi}\varphi_i - \frac{\delta t}{2\tau_\varphi}\varphi_i^{eq} - \frac{\delta t}{2}F_i^\varphi \end{aligned} \tag{24}$$

$$\begin{aligned} \widetilde{\varphi}_i^+ &= \varphi_i + \frac{\delta t}{2}(\Omega_i^\varphi + F_i^\varphi) \\ &= \frac{2\tau_\varphi - \delta t}{2\tau_\varphi + \delta t}\widetilde{\varphi}_i + \frac{2\delta t}{2\tau_\varphi + \delta t}\varphi_i^{eq} + \frac{2\tau_\varphi \delta t}{2\tau_\varphi + \delta t}F_i^\varphi \end{aligned} \tag{25}$$

Then Eq. (20) becomes

$$\widetilde{\varphi}_i^{n+1} = \widetilde{\varphi}_i^{+,n} - \frac{\delta t}{|V_j|} J_\varphi^{n+1/2} \tag{26}$$

In practice, $\widetilde{g}_i$ and $\widetilde{f}_i$ are solved, and the hydrodynamic variables can be obtained as folllows

$$\phi(\boldsymbol{x}_j, t_n + \delta t) = \sum_{i=0}^{q-1} \widetilde{g}_i \tag{27}$$

$$p(\boldsymbol{x}_j, t_n + \delta t) = \sum_{i=0}^{q-1} \widetilde{f}_i + \frac{\delta t}{2} \sum_{i=0}^{q-1} F_i^f \tag{28}$$

$$\rho RT \boldsymbol{u}(\boldsymbol{x}_j, t_n + \delta t) = \sum_{i=0}^{q-1} \boldsymbol{\xi}_i \widetilde{f}_i + \frac{\delta t}{2} \sum_{i=0}^{q-1} \boldsymbol{\xi}_i F_i^f \tag{29}$$

The key step in updating $\widetilde{\varphi}_i^{n+1}$ is to evaluate the flux across the cell interface. According to the above formula, the flux is determined by the original distribution function $\varphi_i(\boldsymbol{x}_b, \boldsymbol{\xi}_i, t_{n+1/2})$ at the half time step. This is done by integrating Eq. (20) for a half time step $h = \delta t/2$ along the characteristic line with the end point located at the center of the cell interface, i.e., $\boldsymbol{x}_b = (\boldsymbol{x}_j + \boldsymbol{x}_{j+1})/2$,

$$\begin{aligned}&\varphi_i(\boldsymbol{x}_b, \boldsymbol{\xi}_i, t_n + h) - \varphi_i(\boldsymbol{x}_b - \boldsymbol{\xi}_i h, \boldsymbol{\xi}_i, t_n)\\ &= \frac{h}{2}[\Omega_i^{\varphi}(\boldsymbol{x}_b, \boldsymbol{x}_i, t_n + h) + \Omega_i^{\varphi}(\boldsymbol{x}_b)] +\\ &\frac{h}{2}[F_i^{\varphi}(\boldsymbol{x}_b, \boldsymbol{\xi}_i, t_n + h) + F_i^{\varphi}(\boldsymbol{x}_b - \boldsymbol{\xi}_i h, \boldsymbol{\xi}_i, t_n)]\end{aligned} \tag{30}$$

Again, two liner transformations are introduced,

$$\bar{\varphi}_i = \frac{2\tau_\varphi + h}{2\tau_\varphi}\varphi_i - \frac{h}{2\tau_\varphi}\varphi_i^{eq} - \frac{h}{2}F_i^{\varphi} \tag{31}$$

$$\bar{\varphi}_i^{+} = \frac{2\tau_\varphi - h}{2\tau_\varphi + h}\bar{\varphi}_i + \frac{2h}{2\tau_\varphi + h}\varphi_i^{eq} + \frac{2\tau_\varphi h}{2\tau_\varphi + h}F_i^{\varphi} \tag{32}$$

Then we obtain

$$\bar{\varphi}_i(\boldsymbol{x}_b, \boldsymbol{\xi}_i, t_n + h) = \bar{\varphi}_i^{+}(\boldsymbol{x}_b - \boldsymbol{\xi} h, \boldsymbol{\xi}_i, t_n) \tag{33}$$

For smooth flows, the right hand side of Eq. (33) can be approximated using Taylor expansion,

$$\bar{\varphi}_i^{+}(\boldsymbol{x}_b - \boldsymbol{\xi} h, \boldsymbol{\xi}_i, t_n) \approx \bar{\varphi}_i^{+}(\boldsymbol{x}_b, \boldsymbol{\xi}_i, t_n) - \boldsymbol{\xi}_i h \cdot \boldsymbol{\sigma}_b \tag{34}$$

where $\boldsymbol{\sigma}_b \equiv \nabla\bar{\varphi}_i^{+}(\boldsymbol{x}_b, \boldsymbol{\xi}_i, t_n)$.
After the update of $\bar{\varphi}_i^{+}(\boldsymbol{x}_b, \boldsymbol{\xi}_i, t_n + h)$ at the cell interface, the hydrodynamic variables at the cell interface at $t_n + h$ can therefore be evaluated as,

$$\phi(\boldsymbol{x}_b, t_n + h) = \sum_{i=0}^{q-1}\bar{g}_i \tag{35}$$

$$p(\boldsymbol{x}_b, t_n + h) = \sum_{i=0}^{q-1}\bar{f}_i + \frac{h}{2}\sum_{i=0}^{q-1}F_i^f \tag{36}$$

$$\rho RT\boldsymbol{u}(\boldsymbol{x}_b, t_n + h) = \sum_{i=0}^{q-1}\boldsymbol{\xi}_i\bar{f}_i + \frac{h}{2}\sum_{i=0}^{q-1}\boldsymbol{\xi}_i F_i^f \tag{37}$$

Thus, the equilibrium distribution function $\varphi^{eq}(\boldsymbol{x}_b, \boldsymbol{\xi}_i, t_n + h)$ can be obtained based on the hydrodynamic variables obtained at the cell interface at $t_n + h$. Then the original distribution functions $\varphi_i(\boldsymbol{x}_b, \boldsymbol{\xi}_i, t_n + h)$ can be obtained,

$$\varphi_i = \frac{2\tau_\varphi}{2\tau_\varphi + h}\bar{\varphi}_i + \frac{h}{2\tau_\varphi + h}\varphi_i^{eq} + \frac{\tau_\varphi h}{2\tau_\varphi + h} + F_i^{\varphi} \tag{38}$$

Now the flux across the cell interface $\boldsymbol{J}_i^{n+1/2}$ can be evaluated by using Eq. (26).
Moreover, due to the nature of linear transformations, the following relations can be derived,

$$\widetilde{\varphi}_i^{+} = \frac{4}{3}\bar{\varphi}_i^{+} - \frac{1}{3}\widetilde{\varphi}_i \tag{39}$$

$$\bar{\varphi}_i^{+} = \frac{2\tau_\varphi - h}{2\tau_\varphi + \delta t}\widetilde{\varphi}_i + \frac{3h}{2\tau_\varphi + \delta t}\varphi_i^{eq} + \frac{3\tau_\varphi h}{2\tau_\varphi + \delta t}F_i^{\varphi} \tag{40}$$

Finally, the distribution function $\widetilde{\varphi}_i^{n+1}$ is updated according to Eq. (20).

Applying the Chapman-Enskog analysis, we can show that the above DUGKS model can yield the following hydrodynamic equations:

$$\rho\left(\frac{\partial \boldsymbol{u}}{\partial t} + \boldsymbol{u}\cdot\nabla\boldsymbol{u}\right) = -\nabla p + \nabla\cdot[\rho\nu(\nabla\boldsymbol{u} + \nabla\boldsymbol{u}^T)] + \boldsymbol{F} \tag{41}$$

$$\frac{1}{\rho c_s^2}\frac{\partial p}{\partial t} + \nabla\cdot\boldsymbol{u} = -\gamma\nabla\cdot(\lambda\nabla\mu_\phi) \tag{42}$$

$$\frac{\partial \phi}{\partial t} + \nabla\cdot(\phi\boldsymbol{u}) = \nabla\cdot(\lambda\nabla\mu_\phi) \tag{43}$$

with the kinematic viscosity ν and the mobility λ expressed by

$$\nu = c_s^2\tau_f, \qquad \lambda = c_s^2\tau_g\eta \tag{44}$$

In the low Mach number limit ($Ma = |\boldsymbol{u}|/c_s$), the hydrodynamic pressure is of order $O(Ma^2)$. Therefore, the above equations are essentially the same as the governing equations in the CHNS system.
A model of the mixture dynamic viscosity is needed to specify the local mixture kinematic viscosity ν as $\nu = \mu/\rho$. The model we adopted is

$$\mu = \frac{\mu_A\mu_B(\phi_A - \phi_B)}{(\phi - \phi_B)\mu_B + (\phi_A - \phi)\mu_A}, \tag{45}$$

which ensures the continuity of viscosity across the interface (Zu & He 2013) , where $\mu_A = \rho_A\nu_A$ and $\mu_B = \rho_B\nu_B$.
In the present study, the D3Q19 lattice particle velocity model is used to set up a 3D simulation code. The same code is used here to generate results for 2D cases (the alternative is to use D2Q9 lattice model). One of the flexibilities in DUGKS is that the time step can be adjusted in terms of the CFL number,

$$\delta t = CFL\frac{\delta x_{min}}{\sqrt{3RT}} \tag{46}$$

where δx_{min} is the minimal grid spacing and the CFL number should be less than one.

Numerical simulation - A 2D stationary droplet

We apply our 3D DUGKS code to simulate a 2D stationary droplet, namely, the variation in the third spatial direction is not present. Initially, a stationary circular droplet is located at the center of the computational domain on a 128×128 mesh. The radius of the droplet R_0 is fixed at 40 lattices units.
According to the phase field approach, the initial phase field is given by

$$\begin{aligned}\phi_0(x, y) &= \frac{\phi_A + \phi_B}{2} + \frac{\phi_A - \phi_B}{2}\\ &\times \tanh\left(2\frac{R - \sqrt{(x - x_c)^2 + (y - y_c)^2}}{W}\right)\end{aligned} \tag{47}$$

where(x_c, y_c) is the center of the droplet. This initial distribution plus zero velocity and zero pressure is used to initialize the fields. The approximate analytical solution based on

the planar interface solution will be used to compare with the numerical results.
The periodic boundary conditions are applied to the four boundaries. Following parameters are used: $\phi_A = 1.0$, $\phi_B = 0.0$, $\rho_A = 1.0$, $\rho_B = 0.2$, $\tau_f = \tau_g = 0.5$, $\sigma = 1 \times 10^{-3}$, $W = 4$, $CFL = 0.25$. Thus, the corresponding dimensionless parameters are $\rho_A/\rho_B = 5$, $\nu_A/\nu_B = 1$, $Ca = \mu_A V_{ref}/\sigma = 33.33$, where $V_{ref} \equiv \sqrt{\sigma R/\rho_A}$. As reported by Zu & He (2013), the mobility needs to be manipulated during the simulation to avoid numerical instability. A very small mobility may cause numerical instability, although the spurious currents and diffusion errors can be reduced with decreasing mobility. Here, after a parametric study, we choose $\lambda = 0.01$ to ensure the better stability. When the droplet reaches the equilibrium state, the phase field at the center line $x = 64$ is shown in Fig. 1, as a function of the normalized distance from the droplet center. We observe that the simulated phase field profile is in excellent agreement with the analytical solution. The maximum relative error between the theoretical and the solution $|\phi_{theory} - \phi|/|\phi_A - \phi_B|$ does not exceed 0.01 in the whole domain.
The pressure difference δP between the inside and outside of the droplet should satisfy the Laplace law, i.e. $\delta P = \sigma/R_0$ when the equilibrium state is reached, where the total pressure P is evaluated as $P = p + p_0 - \kappa\phi\nabla^2\phi - \kappa|\nabla\phi|^2/2$, here $p_0 = \phi d\psi/d\phi - \psi$ is the thermodynamic pressure, p is the hydrodynamic pressure and the other term is related to the curvature. Fig. 2 shows the relationship between the pressure P and the normalized distance from the center of the droplet. The simulated pressure jump is 2.491e-5, which agrees well with the theoretical value σ/R=2.5e-5. We also observe that there exists small fluctuation near the interface and we are studying the origin of this fluctuations.
The comparison of the the thermodynamic pressure p_0 is given in Fig. 3. The $L1$ error is smaller than 1.64%. If we compare $-\kappa\phi\nabla^2\phi$, and $-\kappa|\phi|^2/2$ to the theoretical solution based on the planar case, we observe also an error less than 3%. Figs. 3, 4, and 5 show the thermodynamic pressure p_0, $-\kappa\phi\nabla^2\phi$, and $-\kappa|\phi|^2/2$, respectively, as a function of y/R_0. All are in excellent agreement with the analytical solutions.

To check the balance of the hydrostatic equations, we calculate the pressure gradient ∇p and the potential form of the interface force $F = -\phi\nabla\mu_\phi$. Fig. 6 show the balance between the pressure gradient and the interface force in x direction, similar solution is obtained for y direction (not shown). We conclude that the spurious currents are very weak and do not affect the balance. The maximum of the velocity normalized by V_{ref} is 3.95×10^{-5} .

The results of 3D droplets are similar. Therefore, we do not present them here.

Numerical simulation - 2D Rayleigh-Taylor instability

We next consider the Rayleigh-Taylor instability of an interface between a heavy fluid on the top and a lighter one below within a gravitational field. The initial perturbation grows rapidly and the heavy fluid is observed to penetrate into the

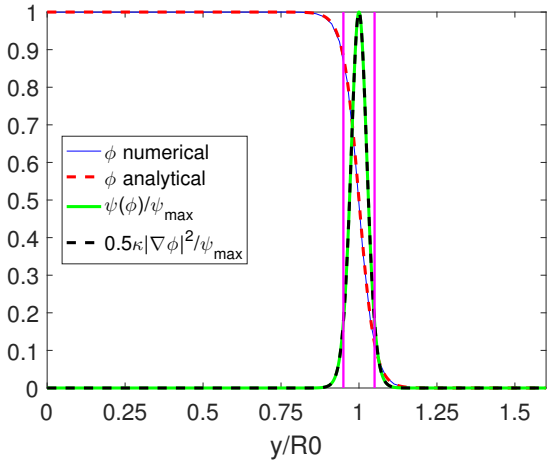

Figure 1: Order parameter ϕ across the interface. Numerical solution and approximate analytical solution across centerline at $x = 64$. The solid green line and the dash black line indicate the analytical solution of the first term and the second term of free energy. The magenta lines indicate the position $(R_0 - W/2)/R_0$ and $(R_0 + W/2)/R_0$ respectively.

lighter fluid producing a complex vortex structure and complex interface shape. The evolution of interface structure and the resultant mixing of two fluids are of great importance in various applications.
The computational domain is set to $[0, L] \times [0, 4L]$ with $L = 256$ lattices units. A heavy fluid with density ρ_A is on the top of a lighter fluid with density ρ_B. The initial interface is located at $\delta(t = 0) = 2L + 0.1L\cos(2\pi y/L)$. The periodic boundary conditions are applied on the lateral boundaries and the bounce back conditions are used on the top and bottom walls.
This problem is governed by three physical dimensionless numbers and they are set as follows: the Atwood number $At = (\rho_A - \rho_B)/(\rho_A + \rho_B) = 0.5$ (which implies that $\rho_A/\rho_B = 3.0$), the ratio of the shear viscosity $\mu_A/\mu_B = 1.0$, and the Reynolds number $Re = \rho_A L\sqrt{gL}/\mu_A = 3000$. In the diffuse interface method, due to the use of Cahn-Hilliard equation, the mobility is considered as a model parameter. Thus, a model dimensionless number, the Pélect number is defined as $Pe = L\sqrt{gL}/\lambda$, where λ is the mobility. For the purpose of code validation, the computational parameters are set to be the same as these of Ren *et al.* (2016), namely, $Pe = 1000$. We choose the reference length equal to the width L, and the reference time equal to $t_{ref} = \sqrt{L/(gA_t)}$. In addition, the width of the interface between two fluids W is fixed to 5 lattice units. A surface tension is fixed with a Eötvos number of $Eo = \frac{\Delta\rho g L^2}{\sigma} = 1747.63$. Since this number is large, one can expect that the flow is driven by the density difference. The CFL number is fixed as 0.25 in the DUGKS simulations.
The time evolution of the position of spike (bottom of the heavier fluid that was moving downward) and bubble (top of the lighter fluid that was rising up) was tracked in our simulation and was compared with data from the literature and

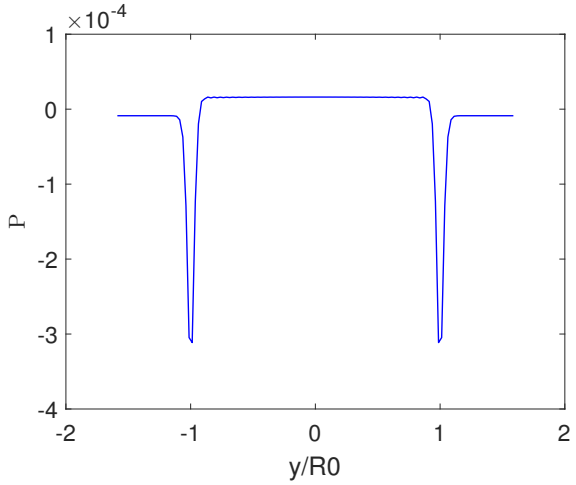

Figure 2: Total pressure P accross the center line at $x = 64$.

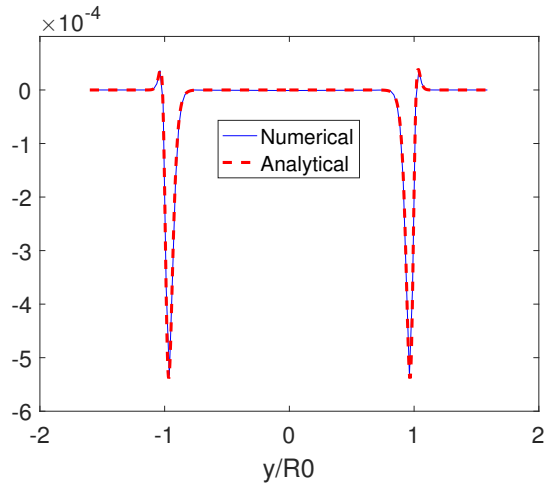

Figure 3: Thermodynamic pressure p_0.

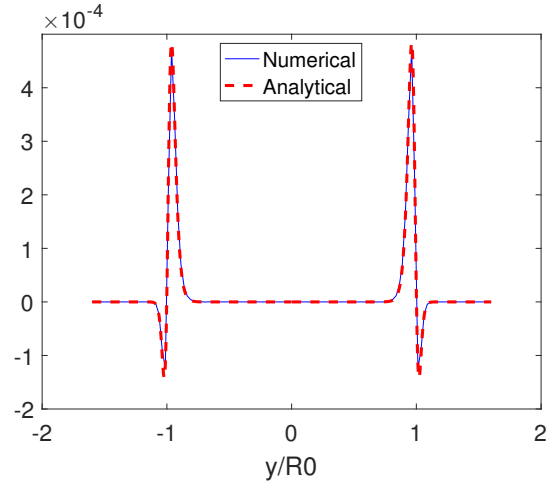

Figure 4: The curvature related part $-\kappa\phi\nabla^2\phi$.

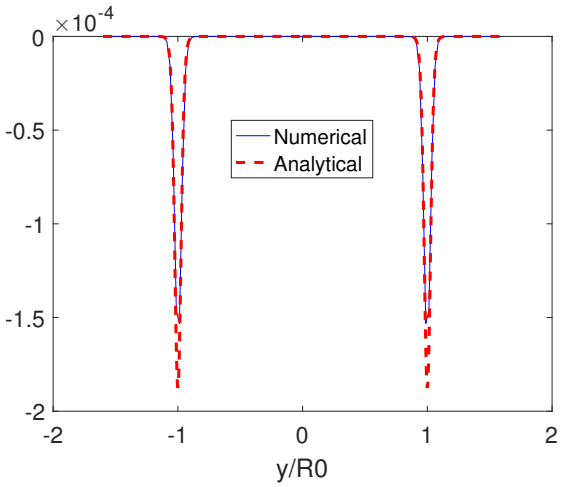

Figure 5: The curvature related part $-\kappa|\nabla\phi|^2/2$.

ARCHER results. Fig. 7 shows the time evolution of the positions of the bubble front and the spike tip, comparing with the data from the literature (Ren *et al.* 2016; Li *et al.* 2012; Ding *et al.* 2007; Zu & He 2013) and ARCHER. The solutions obtained from the literature are all obtained with LBM based solvers with a mesh grid equivalent to the present simulations (between 150 and 256 lattices in the x direction). It is important to remark that the results from (Zu & He 2013; Ding *et al.* 2007) are obtained without surface tension while (Ren *et al.* 2016) is simulated with surface tension. As expected, the small surface tension does not play important role in this case.

The shapes of the interface at different times are displayed in Fig. 8. The orange color represents our results and the green represents the ARCHER results. The results from the two different methods are very similar. At the initial time, the generation of the falling spike of the heavy fluid and the rising bubble of the lighter fluid can be clearly observed. At time continues, mushroom structures are formed due to the well known Kelvin-Helmholtz instability. Later on, complex interactions between two fluids lead to the breakup of the mushroom spike into smaller structures. The differences between both codes for these larger times can be explained by the physical chaotic flow that is very sensitive to small perturbation. At later times we can observe some diffused interface structures in the phase field approach, which is expected. Nevertheless, this diffusion is weak such that the main interfacial instability evolution is unaffected.

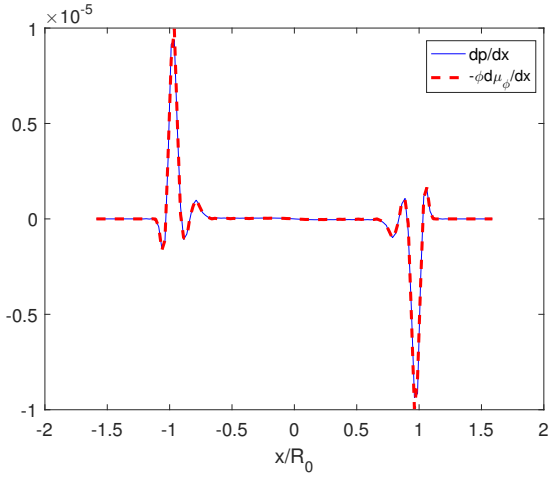

Figure 6: Hydrostatic balance in the x direction, $dp/dx = -\phi d\mu_\phi/dx$.

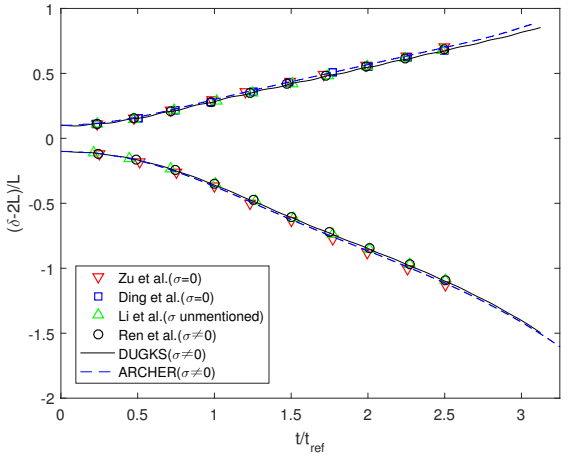

Figure 7: Time evolution of the positions of spike and bubble.

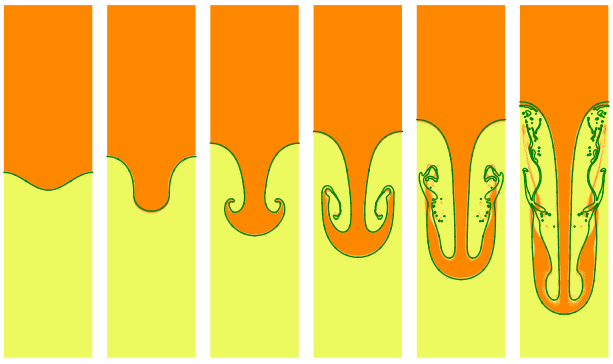

Figure 8: ARCHER Interface (green) on DUGKS Phase Field (background) for: $Eo = 1747.63$, $Re = 3000$, $\rho_A/\rho_B = 3$, $\mu_A/\mu_B = 1$, $At = 0.5$. Times are respectively $t^* = \{0, 1.0, 1.5, 2.0, 2.5, 3.125\}$.

Numerical simulation - 3D Rayleigh-Taylor instability

Following the two dimensional case, next we simulate three dimensional Rayleigh-Taylor instability to demonstrate the capability and accuracy of the DUGKS method. The simulation is performed in a rectangular domain of size $[0, L] \times [0, L] \times [0, 4L]$, with $L = 64$ lattices units. For the convenience of comparison, the model parameters are chosen according to the work of Mitchell *et al.* (2018). It is important to remark that they use a higher resolution of $L = 128$ in their paper. The phenomenon is characterized by several important dimensionless numbers including Atwood number, At, Reynolds number, Re, and capillary number, Ca. They are $At = (\rho_A - \rho_B)/(\rho_A + \rho_B) = 0.5$, $Re = L\sqrt{gL}/\nu = 128$, $Ca = \mu_A\sqrt{gL}/\sigma = 9.1$, respectively. At describes the density ratio, Re indicates the relative effect of gravitational to viscous forces, and Ca is the relative effect of viscous forces to the surface tension force. Here g is the gravitational acceleration, ρ_A and ρ_B are the densities of the heavy fluid and the lighter fluid, respectively. σ is the surface tension. μ_A is the dynamic viscosity of the heavy fluid and μ_B for the lighter fluid. The kinematic viscosities of the two fluids are specified to be equal (i.e., $\nu^* = \nu_A/\nu_B = 1$) and thus $\mu^* = \mu_A/\mu_B = 3$. The Eötvos number here is 776.53. As in the 2D case, the density ratio drives the instability process. Additionally, $Pe = L\sqrt{gL}/\lambda = 744$ is the numerical Péclet number, λ is the mobility in the Cahn-Hilliard equation. The reference time is defined as $t_{ref} = \sqrt{L/g} = 6000$ such that the dimensionless time is $t^* = t/t_{ref}$. The no-slip bounce back conditions are applied on the top and bottom walls while periodic boundary conditions are used on the other two directions. The initial interface position between the heavy fluid and lighter fluid is given by a single mode perturbation, i.e., $\delta(y, z) = 2L + 0.05L[\cos(2\pi y/L) + \cos(2\pi z/L)]$.

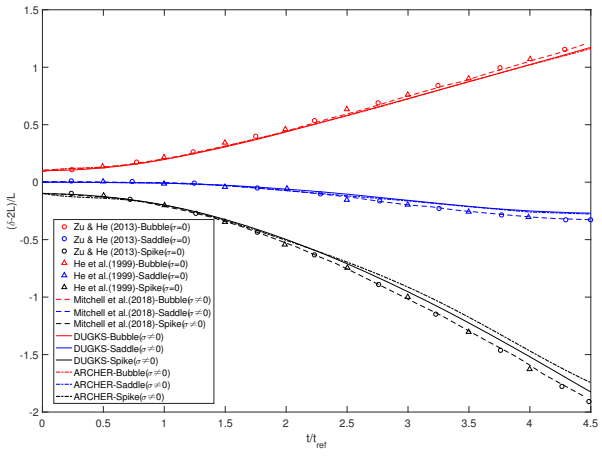

Figure 9: Time evolution of the positions of the bubble front, the saddle point and the spike in the case of Rayleigh-Taylor instability.

A quantitative comparison is performed by tracking the position of the bubble, spike, and saddle points through the simulation. Fig. 9 shows time evolution of the positions of

the bubble front, the saddle points and the spike obtained from the literature, DUGKS and ARCHER. Finally, we have to point out that the cases in Zu & He (2013), He *et al.* (1999) were done without surface tension, while the case in Mitchell *et al.* (2018) was done with surface tension. For the bubble front and saddle locations, DUGKS and ARCHER are in excellent agreement. The zero-surface-tension solutions for the bubble front are slightly higher and slightly lower for the saddle. This was expected since the surface tension tends to stabilize the Rayleigh-Taylor instability. If we focus on the spike, where the differences are more clearly seen, DUGKS and ARCHER are also in excellent agreement at early times. At later times, DUGKS predicts a lower spike location, perhaps due to different levels of numerical dissipation in DUGKS and ARCHER. The results of Mitchell *et al.* (2018) considering surface tension appear to match those obtained without surface tension. Given that DUGKS and ARCHER are in good agreement, we have confidence in our results. Further simulations at higher grid resolutions are needed to clarify the differences caused by the surface tension. Overall, here the stabilization effect of surface tension is weak, when compared to the unstable effect due to the differential gravity.

Numerical simulation - Two-phase decaying homogeneous isotropic turbulence

Finally, we perform a direct numerical simulation of two-phase decaying homogeneous isotropic turbulence with fluid-fluid interfaces. The aim of present work is to validate the DUGKS code thus only preliminary results are shown here.
The computational domain is a cubic box with periodic boundary conditions in all three directions. The spatial grid resolution is 128^3 lattices. In DNS of homogeneous isotropic turbulence, an adequate grid resolution is of primary importance. The Kolmogorov scale η in the carrier phase and the smallest scale of liquid structures should be resolved. For the single phase case, Wang *et al.* (2016) has shown that the DUGKS has a superior numerical stability particularly for high Reynolds number flows and can adequately resolve the flow when $k_{max}\eta > 3$, where k_{max} is the maximum resolved wave number and η is the Kolmogorov length scale. In our simulation, the initial $k_{max}\eta = 7.0$. Here the density ratio and the viscosity ratio are both set to unity in order to get rid of the influence of the density ratio and the viscosity ratio. The CFL number is 0.25. The initial maximum velocity magnitude is 0.034. The surface tension is $\sigma = 1 \times 10^{-20}$ ($We = \rho u_{rms}^2 R/\sigma = 2.48 \times 10^{17}$).
We consider initially a single drop in a turbulent flow field obtained with linear forcing scheme (Rosales *et al.* 2005; Duret 2012). In order to set up a physically initial velocity field across the droplet interface that is not subjected initially to high shear flow, we first run a forced homogeneous isotropic turbulence to create a developed single phase turbulent velocity field. Then we add a solid particle to the flow field. After several large eddy turnover times, we extract this velocity field and use it to initialize the two-phase flow. This initialization was done with the ARCHER code, where the solid particle was treated by an Immersed Boundary Method (Breugem 2012). This initial condition was shared among both codes. For the DUGKS code, we add the non-equilibrium part of the distribution function to initialize the new distribution functions $\tilde{f}$ and $\tilde{g}$ through the Chapmann-Enskog analysis. The initial radius of the droplet is 31.7 lattice units ensuring a good resolution of the flow inside the droplet. The volume fraction V_{drop}/V_{box}= 0.064. The slices of the contour of the normalized velocity magnitude $|\boldsymbol{u}|/|\boldsymbol{u_0}|_{max}$ and vorticity magnitude $|\boldsymbol{\omega}|/|\boldsymbol{\omega_0}|_{max}$ at different times are shown in Fig. 10 and Fig. 11, respectively.

We can observe that the complexity of the interface increases with time, which is well represented by the phase field approach. The study of this interface evolution, in particular under more harsh conditions (*e.g.*, higher density ratio, higher surface tension), is very relevant to the practical atomization process (Canu *et al.* 2018). These conditions remain a challenge topic for our DUGKS-phase field approach, which deserves further investigation.

The quantitative comparisons of the velocity magnitude and the vorticity magnitude on a line at $z = 63.5, x = 63.5$ are also shown in Fig. 12. The results from DUGKS agree well with the results from ARCHER. We note that both DUGKS and ARCHER are designed to be of the second-order accuracy.

Conclusions

We have developed a three dimensional DUGKS code and use it to simulate both two-dimensional and three-dimensional immiscible two-phase flows. The cases considered include a stationary droplet, the Rayleigh-Taylor instability, two-phase homogeneous isotropic decaying turbulence in order of complexity. The results obtained by the DUGKS are compared to those from the literature and the ARCHER code based on the Coupled Level Set - Volume of Fluid (CLSVOF) method. The results demonstrate the reliability of DUGKS. Future studies will focus on the physical evolution of immiscible two-phase flows as related to the secondary breakup dynamics of a drop in a turbulent background flow. In the present communication we have focused on physical cases where the surface tension is not the main parameter driving the flow. In this study we show that the combined phase field and DUGKS approach provides reliable results. Ongoing work addresses cases where surface tension is the main parameter. Results are promising and encourage us to go further on DUGKS method for the treatment of immiscible two-phase flows. We note that there appears to be very few studies combining mesoscopic methods and the phase field approach for turbulent immiscible two-phase flow, and the only work known to us is Komrakova *et al.* (2015). The DUGKS code will also need to be optimized in terms of computational efficiency and numerical accuracy.

Acknowledgments

This work has been supported by the National Natural Science Foundation of China (91852205 & 91741101), and by the U.S. National Science Foundation (NSF) under grants CNS1513031 and CBET-1706130.

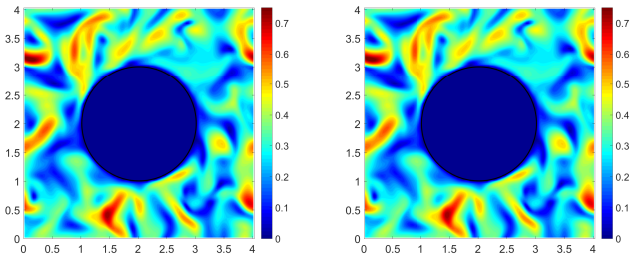

(a) $t^* = 0$

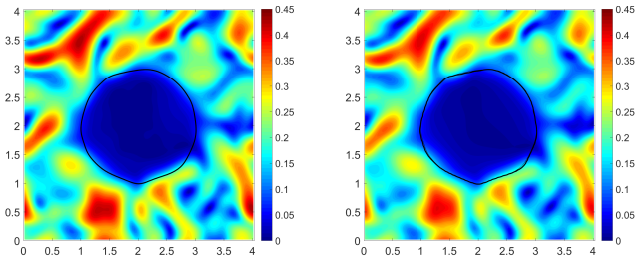

(b) $t^* = 0.98$

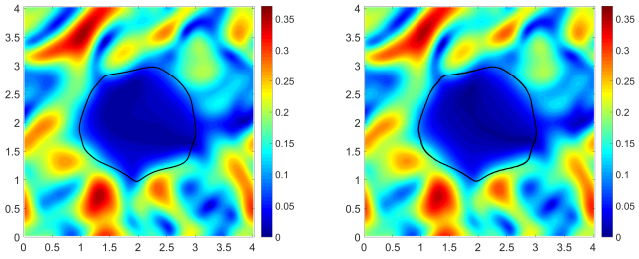

(c) $t^* = 1.96$

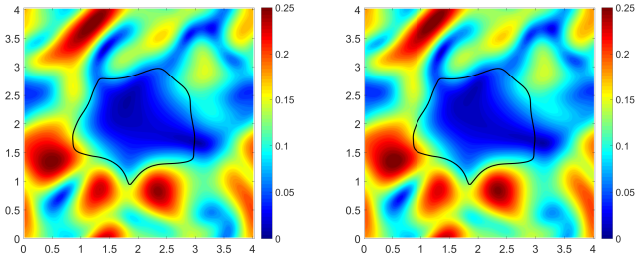

(d) $t^* = 3.91$

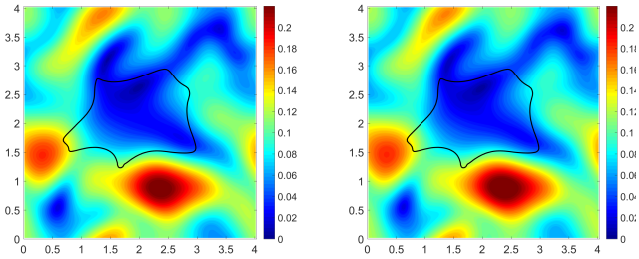

(e) $t^* = 7.83$

Figure 10: Contours of normalized velocity magnitude $|\boldsymbol{u}|/|\boldsymbol{u_0}|_{max}$ at dimensionless time $t^* = t\epsilon_0/K_0$=0, 0.98, 1.96, 3.91, and 7.83 with $N^3 = 128$. Left: DUGKS, Right: ARCHER. The solid black line indicates the interface position. The colorbar indicates the relative magnitude of the velocity field.

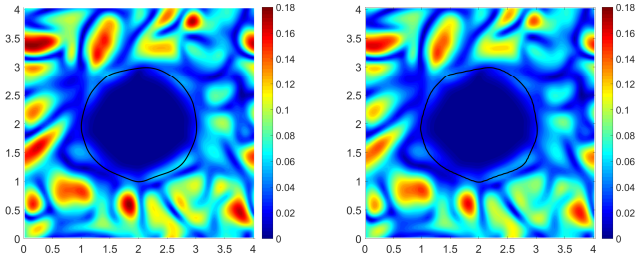

(a) $t^* = 0.98$

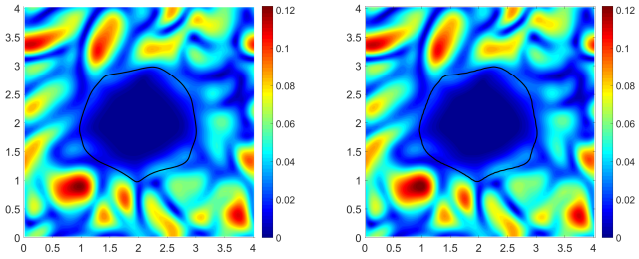

(b) $t^* = 1.96$

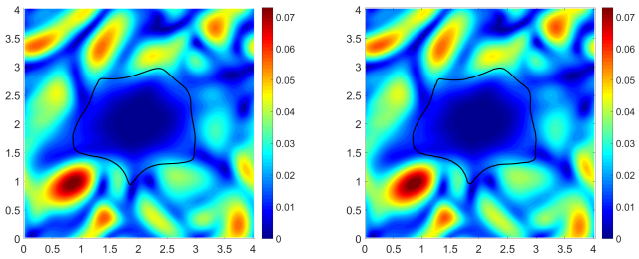

(c) $t^* = 3.91$

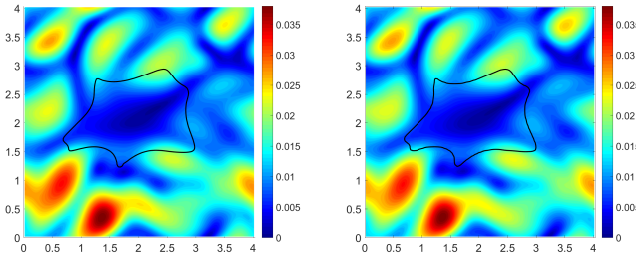

(d) $t^* = 7.83$

Figure 11: Contours of normalized vorticity magnitude $|\boldsymbol{\omega}|/|\boldsymbol{\omega_0}|_{max}$ at dimensionless time $t^* = t\epsilon_0/K_0$=0, 0.98, 1.96, 3.91, and 7.83 with $N^3 = 128$. Left: DUGKS, Right: ARCHER. The solid black line indicates the interface position. The colorbar indicates the relative magnitude of the vorticity field.

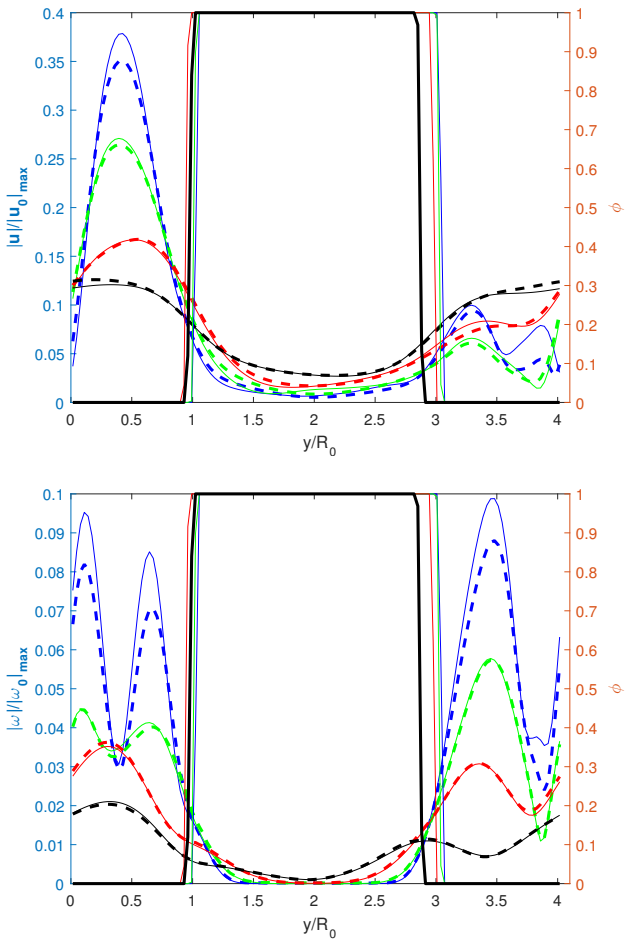

Figure 12: Curves of normalized velocity magnitude $|\boldsymbol{u}|/|\boldsymbol{u_0}|_{max}$ (top) and vorticity magnitude (top) $|\boldsymbol{\omega}|/|\boldsymbol{\omega_0}|_{max}$ (bottom) at dimensionless time $t^* = t\epsilon_0/K_0$= 0.98 (blue), 1.96 (green), 3.91 (red), and 7.83 (black) with $N^3 = 128$, cutting through $z = 63.5, x = 63.5$. Solid line: DUGKS, dash line: ARCHER. The line with a corresponding color indicates the interface position given by ARCHER.

References

Guo, Z.L., Xu, K.,Wang, R. Discrete unified gas kinetic scheme for all Knudsen number flows: low-speed isothermal case. Phys. Rev. E, Vol. 88: 033305 (2013)

Guo Z.L., Wang R., Xu K. Discrete unified gas kinetic scheme for all Knudsen num- ber flows. II Thermal compressible case. Phys. Rev. E, Vol. 91: 033313 (2015)

Wang, P., Wang, L.-P., Guo, Z.L. Comparison of the lattice Boltzmann equation and discrete unified gas-kinetic scheme methods for DNS of decaying turbulent flows. Phys. Rev. E, Vol. 94: 043304 (2016)

Bo, Y.T., Wang, P., Guo, Z.L., Wang, L.-P. DUGKS simulations of three-dimensional Taylor-Green vortex flow and turbulent channel flow. Computers & Fluids, Vol. 155, pp. 9-21 (2017)

Zhang, C.H, Yang, K., Guo, Z.L. A discrete unified gas-kinetic scheme for immiscible two-phase flows. Int. J. Heat & Mass Transfer, Vol. 126, pp. 1326-1336 (2018)

Zu, Y. & He, S. Phase-field-based lattice Boltzmann model for incompressible binary fluid systems with density and viscosity contrasts. Phys. Rev. E, Vol. 87: 043301 (2013)

Ren, F., Song, B., Sukop, M.C., Hu, H. Improved lattice Boltzmann modeling of binary flow based on the conservative Allen-Cahn equation. Phys. Rev. E, Vol. 94: 023311 (2016)

Li, Q., Luo, K.H., Gao, Y.J. , He, Y.L. Additional interfacial force in lattice Boltzmann models for incompressible multiphase flows. Phys. Rev. E, Vol. 85: 026704 (2012).

Ding, H., Spelt, P.D.M., Shu, C. Diffuse interface model for incompressible two-phase flows with large density ratios. J. Comp. Phys., Vol. 226, pp. 2078-2095 (2007)

Mitchell, T., Leonardi, C., Fakhari, A. Development of a three-dimensional phase-field lattice Boltzmann method for the study of immiscible fluids at high density ratios. Int. J. Multiphase Flow, Vol. 107, pp. 1-15 (2018)

He, X., Zhang, R., Chen, S., Doolen, G.D. On the three-dimensional Rayleigh-Taylor instability. Phys. Fluids, Vol. 11, pp. 1143-1152 (1999)

Ménard, T., Tanguy, S., Berlemont, A. Coupling level set/VOF/ghost fluid methods: Validation and application to 3D simulation of the primary break-up of a liquid jet. Int. J. Multiphase Flow, Vol. 33, pp. 510-524 (2007)

Komrakova, A.E., Eskin, D., Derksen, J.J. Numerical study of turbulent liquid-liquid dispersions. AIChE J., Vol. 61, pp. 2618-2633 (2015)

Vaudor, G., Ménard, T., Aniszewski, W., Doring, M., Berlemont, A. A consistent mass and momentum flux computation method for two phase flows. Application to atomization process. Computers & Fluids, Vol. 152, pp. 204-216 (2017)

Breugem, W. P., A second-order accurate immersed boundary method for fully resolved simulations of particle-laden flows. J. Comp. Phys., Vol. 231, pp. 4469 - 4498 (2012)

Canu, R., Puggelli, S., Essadki, M., Duret, B., Ménard, T., Massot, M., Reveillon, J., Demoulin, F-X., Where does the droplet size distribution come from? Int. J. Multiphase Flow, Vol. 107, pp. 230-245 (2018)

Rosales, C., Meneveau, C. Linear forcing in numerical simulations of isotropic turbulence: physical space implementations and convergence properties. Phys. Fluids, Vol. 17, pp. 95-106 (2005)

Duret, B., Luret, G., Reveillon, J., Ménard, T., Berlemont, A., Demoulin, F-X. DNS analysis of turbulent mixing in two-phase flows. Int. J. Multiphase Flow, Vol. 40, pp. 93-105 (2012)